Effect of wettability on two-phase quasi-static displacement: validation of two pore scale modeling approaches

Rahul Verma[a], Matteo Icardi[b,c,d], Maša Prodanović[a]

[a] *Petroleum and Geosystems Engineering, University of Texas at Austin, 200 E Dean Keaton, Stop C0300, Austin, TX 78712-1585, USA*
[b] *Mathematics Institute, Zeeman Building, University of Warwick, Coventry, CV4 7AL*
[c] *Division of Computer, Electrical and Mathematical Sciences and Engineering, King Abdullah University of Science and Technology, 23955-6900 Thuwal, Saudi Arabia*
[d] *Institute of Computational Engineering and Sciences, University of Texas at Austin, TX 78712-1585, USA*

Abstract

Understanding of pore-scale physics for multiphase flow in porous media is essential for accurate description of various flow phenomena. In particular, capillarity and wettability strongly influence capillary pressure-saturation and relative permeability relationships. Wettability is quantified by the contact angle of the fluid-fluid interface at the pore walls. In this work we focus on the non-trivial interface equilibria in presence of non-neutral wetting and complex geometries. We quantify the accuracy of a volume-of-fluid (VOF) formulation, implemented in a popular open-source computational fluid dynamics code, compared with a new formulation of a level set (LS) method, specifically developed for quasi-static capillarity-dominated displacement. The methods are tested in rhomboidal packings of spheres for a range of contact angles and for different rhomboidal configurations and the accuracy is evaluated against the semi-analytical solutions obtained by Mason and Morrow (1994). While the VOF method is implemented in a general purpose code that solves the full Navier-Stokes (NS) dynamics in a finite volume formulation, with additional terms to model surface tension, the LS method is optimised for the quasi-static case and, therefore, less computationally expensive. To overcome the shortcomings of the finite volume NS-VOF system for low capillary number flows, and its computational cost, we introduce an overdamped dynamics and a local time stepping to speed up the convergence to the steady state, for every given imposed pressure gradient (and therefore saturation condition). Despite these modifications, the methods fundamentally differ in the way they capture the interface, as

Preprint submitted to Journal of Contaminant Hydrology *October 2, 2017*
Email address: rahulverma86@gmail.com (Rahul Verma)

well as in the number of equations solved and in the way the mean curvature (or equivalently capillary pressure) is computed. This study is intended to provide a rigorous validation study and gives important indications on the errors committed by these methods in solving more complex geometry and dynamics, where usually many sources of errors are interplaying.

---

1. Introduction

In this work, we focus on the displacement of two immiscible phases in the subsurface, under variable wettability conditions, for example, in the context of movement of oil and water in hydrocarbon reservoirs, or water and non-aqueous phase liquids (NAPL) in soil. Wettability, as quantified by the contact angles, influences oil and gas recovery processes like waterflooding [1, 2] and other subsurface flow fields like carbon sequestration [3, 4], pollutant migration and remediation processes in subsurface, transport of dissolved minerals, colloids or contaminants, in dissolution and precipitation processes, modeling of groundwater aquifers and so on [5].

Wettability is affected by rock mineralogy, organic deposits like bitumen, and surface roughness of the rocks [1]. Given the complexity of capturing this in a real rock, all modeling studies resort to simplifications. Field scale simulators use averaged flow equations like Darcy's law in combination with mass conservation to model flow. In these simulators, wettability is incorporated into a J-function, which relates the capillary pressure and saturation in a given porous medium [6, 7, 8]. The J-function is an empirical relationship whose parameters are fit to experiments, and is therefore only indirectly related to the actual contact angle at the pore scale. As such, it is difficult to relate spatial and temporal wettability changes in the porous medium to the final J-function for the representative elementary volume (REV). For a more detailed study, one can focus on a much smaller system - modeling flow in individual rock pores. These pore scale studies can be performed on two or three dimensional images of small rock samples. Upon obtaining the detailed pore structure of a rock via techniques such as X-ray microtomography [9], there are multiple approaches for simulating flow (for a review see Meakin and Tartakovsky [10]). There exist two broad categories of methods: direct simulation on the pore image, or simplifying the image into a network of simplified pores (openings) and throats (tight spots). The latter speeds up simulations due to analytical solutions for flux through each throat [11], allowing simulations over larger volumes than those used in direct simulation. There is a lot of network modeling work for wettability problems [11], but that is outside the scope of this work.

For direct simulations, the most popular methods are Navier-Stokes based solvers [5]. Here, the full Navier-Stokes equations are solved in the pore space with an additional equation for the interface and additional terms to model surface tension forces. They are based on discretizing the flow domain into a computational grid. The finite-volume discretization can handle very complex computational grids (e.g., with arbitrary shaped cells, and lo-

cal or adaptive refinements), but building the grids can be considered a delicate separate modeling step that requires accurate validation [12]. This, together with their direct applicability on voxelized rock microstructure images, is the reason why simpler uniform Cartesian grids have gained popularity. These are generally less accurate due to the poor representation of the curved boundaries and the absence of local refinements. However they can have important advantages in data storage and parallelization. The lattice Boltzmann method, for example, is based on such a discretization [5]. One of the problems associated with the direct simulation of pore images is the intrinsic difficulty in a robust validation, which is able to distinguish between the several sources of errors and uncertainties associated with the image pre-processing, sample size, geometry and equation discretization [13]. This is an important reason to further develop benchmark and validation studies for geometries described analytically, like the one proposed in this work. Despite these challenges, pore scale simulation enables improvements of macroscopic models by taking into account different factors like topology of the medium, heterogeneities, and changes in wettability.

In multiphase flow pore scale simulations, the interface represents a moving discontinuity in the domain and is difficult to handle numerically. In this paper, we consider two techniques for modeling interface movement: a variational formulation of the level set method [14], and the volume of fluid method, implemented in the interFoam solver, slightly modified starting from the version released within OpenFOAM 2.3.0. The level set method was first proposed by Osher and Sethian in their seminal work [15]. The method has since been applied for a wide variety of applications: from image-processing and modeling flames to multiphase flows, and was introduced to model quasi-equilibrium fluid/fluid interface movement in porous media by Prodanović and Bryant [16]. The method was used for simulating drainage and imbibition in a porous medium of arbitrary geometry, when the contact angle is zero. By defining the location and propagation of the interface in an implicit manner, the level set method automatically handles operations such as interface splitting and merging. This is particularly useful for tracking movement of an interface in a porous medium where phenomena like snap-off and trapping often take place. Doing this using an explicitly defined interface, such as by front tracking, would be generally more time consuming, due to interface complexity in the pore space [17]. The level set method has already been widely used for two-phase flow applications for incompressible fluid flow [18]. Zhao *et al.* [19] proposed a variational approach for problems involving solid and fluid domains with different surface and bulk energies. The level set method can also be extended for modeling

flow of more than two phases, for example by representing each interface by its own level set function [20]. Level set methods suffer from mass loss, especially in underresolved regions. Enright *et al.* [21] addressed it using a modification called the particle level set method. For further details about the level set method we refer to the textbooks by Osher and Sethian on the topic [22, 23].

The other technique we are using is a classical fluid dynamics solver combined with a volume of fluid (VOF) method [24] for interface propagation. At its core, VOF is similar to level set techniques. The original geometric version of VOF uses explicit reconstruction of the interface in each cell (e.g., the so-called Piecewise-Linear Interface Calculation (PLIC) VOF), while the algebraic version implemented in the open-source code OpenFOAM is, in our opinion, preferable when complex meshes with arbitrary shaped cells are unavoidable. This method has been recently used for pore-scale simulations by many authors [25, 26, 27, 28, 29]. The main limitation of this implementation is the appearance of "parasitic" (or "spurious") currents that can significantly affect the accuracy near the interface. These unphysical velocity oscillations typically scale as the inverse of the capillary number (ratio of viscous to capillary forces) and cannot be removed by refining the mesh. They are caused by the continuous representation of surface tension forces, across the discontinuity represented by the interface.

Some earlier works have focused on comparison of the level set method's accuracy with respect to the volume of fluid method in classical two-phase flow benchmarks. For example, Sussman and Puckett (2000) [30] compared the two methods, and proposed a coupled level set and volume of fluid method. A later validation work was done by Gerlach *et al.* (2006) [31], who studied an equilibrium rod, a capillary wave and the Rayleigh-Taylor instability to compare three different volume of fluid formulations. Some other authors have commented on the accuracy of the volume of fluid method for capturing curvatures ([22]), which are independent of the capillary number effects, but the volume of fluid method has also evolved since then, and contemporary validation exercises have not been carried out. A more recent validation effort was by Rabbani *et al.* [32], who calculated drainage curvatures using the volume of fluid method in simple, constant cross section geometries of the type used in pore network models. However, they did not report on any parasitic currents which typically appear for low capillary number flows.

The objective of this work is to perform a validation study in capillary dominated slow displacement (where the interface can be considered in equilibrium) under uniform wettability conditions in geometries where

either analytical solutions or reliable experimental data is available. We consider the semi-analytical solutions in simple 3D geometries formed by different sphere arrangements by Mason and Morrow [33]. These analytical solutions, derived from further geometrical simplifications, were proven to be very accurate for a wide range of contact angles and geometrical parameters, through validation against experimental curvature measurements. We note that when Jettestuen *et al.* first proposed the variational formulation for contact angles, they did carry out a validation exercise. However, they only did it for either 2D cases, or for 3D cases of constant cross-section. We demonstrate that the formulation needs an additional modification in order to get good results for 3D geometries of non-uniform cross-sections. This simple, yet three-dimensional, set of pore geometries are ideal for validation of numerical methods. A large amount of experimental work exists using micromodels [34], X-ray computed microtomography [35, 9] and on the lab scale [36, 37, 38]. X-ray tomography allows for direct imaging of fluid distributions in more complex geometries, including finding local contact angles ([39, 40, 41]), in 3D. However, the experiments are non-trivial and flow field, contact angles and correct curvatures in tighter pore spaces are still difficult to map, which makes inter-comparison with simulation challenging. Our work here is a step in that direction.

We present here results for two commonly used approaches, namely an equilibrium level set formulation, and a full Navier-Stokes model with algebraic VOF method. The latter, despite being designed for more general dynamic calculations, is here modified to be able to compute efficiently the steady state (equilibrium) through an over-damped pseudo-time stepping. This is, to the authors' knowledge, the first attempt to validate these two interface tracking methods with analytical results in an asymmetric, converging-diverging geometry, typical in realistic porous media. The results can help assess the accuracy and usability of these methods for more complex problems or random wettability patterns, and for upscaling capillary pressure models in Darcy-scale equations. The critical curvatures for drainage obtained by these models can also serve as input for drainage in throats in pore network models.

There are some other works based on the lattice Boltzmann method, which incorporate uniform and mixed wettability for predicting relative permeability in porous media [42, 43]. However, they do not make attempts to validate small-scale multiphase displacements in a converging-diverging porous media geometry. Validation is usually done using a drop on flat surface, or a straight duct [44].

2. Methods

2.1. The level set method, with imposition of contact angle

The method introduced by Prodanovič and Bryant [16] models displacement of immiscible fluids with zero contact angles in arbitrarily complex geometries. It is based on the following level set evolution equation:

$$\partial_t \phi + (a - b\kappa)|\nabla\phi| + \vec{V} \cdot \nabla\phi = 0 \tag{1}$$

The level set function ϕ is defined at each grid point throughout the domain of interest as the distance from the wetting/non-wetting fluid interface, which is the zero level set. The level set function ϕ is defined such that it is positive "outside", or on the side on convexity, and negative on the concave side. For instance, in a two-phase porous media formulation, $\phi > 0$ could denote the wetting phase, and $\phi < 0$ denotes the non-wetting phase and solid grain together (the choice of sign is, of course, arbitrary). As the interface advances, the ϕ function is updated throughout the domain according to the level set equation. Defining the interface implicitly means that changes in the topology of the fluid phases, such as snap-off and merging of fluid menisci, are handled automatically.

Equation (1) governs the evolution of the function ϕ in space while imposing interface speed. The term a is the speed of the interface normal to itself - it can be viewed as a pressure-like term. The curvature-dependent term $b\kappa$ acts opposite to the imposed normal speed a. b determines how strong the effect of curvature is - it is an interfacial tension-like term, and is always positive for stability of the numerical method. $\vec{V}$ represents the external advective field. The pore-grain boundary is defined by a separate level set function ψ, such that the boundary is where $\psi = 0$.

Based on Equation (1), Jettestuen *et al.* [14] proposed a variational approach to model contact angles in porous media. In their formulation, in the main pore space, the sum $a - b\kappa$ represents the difference between imposed capillary pressure and the surface tension force (reproducing the Young-Laplace equation), while near the boundaries, a, b and $\vec{V}$ are modified to impose contact angles. We adopt their approach to get the following modified level set equation:

$$\begin{aligned} \phi_t + \{H(-\psi)\kappa_0 - S(\psi)H(\psi)Ccos\beta|\nabla\psi|\}|\nabla\phi| \\ + S(\psi)H(\psi)C\nabla\psi \cdot \nabla\phi = H(-\psi)\kappa_\phi|\nabla\phi| \end{aligned} \tag{2}$$

Here, $H()$ denotes a Heaviside function, and is given by:

$$H(\psi) = \begin{cases} 0, & \psi < 0 \\ \frac{1}{2} + \frac{\psi}{2\epsilon} + \frac{1}{2\pi} sin\left(\frac{\pi\psi}{\epsilon}\right), & -\epsilon \leq \psi \leq \epsilon \\ 1, & \psi > \epsilon \end{cases} \tag{3}$$

where ϵ is set to $1.5\Delta x$, and Δx is the numerical cell length. Terms meant to take effect in the pore space are multiplied by $H(-\psi)$, whereas the solid phase terms are multiplied by $H(\psi)$. $\theta = \pi - \beta$ is the contact angle imposed on the medium (see Figure 1), where β is the angle enclosed by the normals $\vec{n}_\phi$ and $\vec{n}_\psi$. Thus, the modified level set equation works by imposing a velocity near the contact line such that the direction of the velocity vector and the gradient vector of the mask form the desired contact angle. Away from the boundary, we impose only the Young-Laplace equation. The diffusive term associated with the zero level set curvature κ_ϕ in Equation (2) smooths the level set function so that we get one single smooth interface despite having different speeds of propagation of the interface near and far from the boundary. The curvature κ_ϕ is given by:

$$\kappa_\phi = \nabla \cdot \frac{\nabla\phi}{|\nabla\phi|} \tag{4}$$

κ_0 is the imposed normal speed on the interface in the pore space. This is slightly different from the quantity a in the original level set equation, as a includes terms both in the pore space and near the boundary. S() is the sign function which ensures that the contact angle propagates away from the walls, and hence ensures numerical stability,

$$S(\phi) = \frac{\phi}{\sqrt{\phi^2 + |\nabla\phi|^2(\Delta x)^2}} \tag{5}$$

C is a constant that was used in Jettestuen *et al.* [14] to scale the contact angle and curvature parts of the velocity. By trial and error, we found it enough to set it equal to one. The level set equation must also be periodically reinitialized to make sure that the gradients in ϕ do not become too large. The default reinitialization equation was used, and is given by:

$$\phi_t + S(\phi)(|\nabla\phi| - 1) = 0 \tag{6}$$

By imposing different values of the contact angle at different locations, mixed wettability conditions can be simulated. A simple example is shown in Jettestuen *et al.* [14], but we do not use it here.

Initially, we introduce a meniscus of low initial curvature into the domain, and advance it until it reaches an equilibrium position in the given

geometry. The speed at which the meniscus approaches the pore throat must be low enough so that it does not simply exit the simulation volume without reaching an equilibrium position. This is different from the compressible model used by Prodanović & Bryant [45], but it does not affect the ultimate critical curvature.

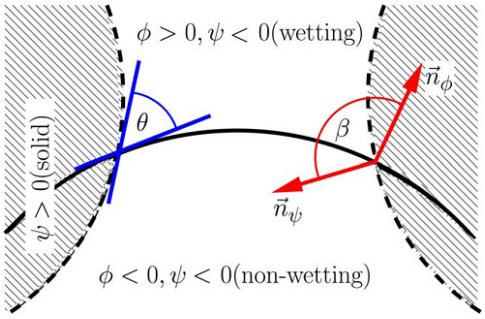

Figure 1: Imposition of contact angle using level set methods.

To simulate a drainage process, at every step, the curvature is increased by $\Delta\kappa$ until the steady state solution is found. Therefore, the "time" t defined in Equation (1) is a parameter without physical meaning.

Masking is enforced at every time step with some overlap, so that, $\phi(x,t) + p \leq \psi$, where p is the overlap, measured in the grid spacing Δx. This is a key difference in our methodology versus that introduced in Jettestuen *et al.* [14]. They also have an overlap in the main equation, but it is not enforced during the masking process. The overlap was found necessary for accuracy as the contact angle became larger. When the contact angle is closer to 0°, no overlap was necessary. As the contact angle increased (beyond 30°), the overlap between the pore space and the grain space was increased gradually, up to a maximum overlap of one grid cell. For 40°, the overlap was 0.3 grid cells, then for contact angle 50° it was 0.5, and finally the overlap was increased to one grid cell by contact angle 60°, and held constant for greater angles. The method is stable without this overlap, but it gave a much better match to analytical values. Having an overlap is not physical. However, it allows for formation of contact angles between different interfaces (the cusp is not a possible solution to a level set equation that contains a diffusive curvature term) and does not affect the equilibrium solution as long as overlap regions belonging to two portions of grain boundary do not touch. It is thus intuitive that the size of the overlap is related to the contact angle.

An imbibition simulation would proceed by taking the endpoint of a

drainage simulation as the starting point. Curvature is decreased step by step, just as it was increased for the previous case. In this work, we have not performed any imbibition simulations.

The equation was solved using the MATLAB level set toolbox written by Ian Mitchell [46, 47]. The time derivative is approximated with a third-order accurate total variation diminishing (TVD) Runge-Kutta integration scheme. The Courant-Friedrichs-Lewy (CFL) conditions restrict the size of the timestep. For the normal and convective terms, the gradients are approximated by an upwind third order accurate essentially non-oscillatory (ENO) finite difference scheme. The WENO (weighted essentially non-oscillatory) scheme is more accurate, but it did not improve the quality of our results, so we use the ENO scheme throughout. For the curvature velocity term, the mean curvature κ is approximated using a centered second order accurate finite difference approximation. This is also used in post-processing the results when we want to compute the distribution of curvature values on the interface. Finally, as explained earlier, the level set equation is reinitialized every few time steps using the reinitialization equation in order to maintain $|\nabla\phi| = 1$. Further details of individual numerical schemes can be found in the book by Osher and Fedkiw [22].

2.2. Finite volume and volume-of-fluid methods

The volume of fluid method is a numerical technique used in the open source software OpenFOAM to track interfaces in multiphase flows. In this implementation the location and velocity of the fluid/fluid interface is updated by using the Navier-Stokes equations, in a coupled manner. The motion of a single incompressible fluid is governed by the Navier-Stokes equation along with the mass conservation equation. For incompressible fluids, the mass conservation equation is given by:

$$\nabla \cdot (\vec{u}\rho) = 0 \tag{7}$$

The Navier-Stokes equation on the other hand describes conservation of momentum:

$$\frac{\partial \rho \vec{u}}{\partial t} + \nabla \cdot (\rho \vec{u}\vec{u}) = -\nabla p + \nabla \cdot (2\mu \vec{E}) + \vec{f_b} \tag{8}$$

Here, ρ, $\vec{u}$ and μ describe the density, velocity field and viscosity of the fluid, respectively. $\vec{E}$ is the rate of strain tensor, while p is the pressure field. $\vec{f_b}$ is the external body force term, which can include gravity. So, in the case of two immiscible fluids, the Navier-Stokes equation along with mass conservation are solved for each fluid separately.

At the interface between the fluids, we need to impose continuity of velocity and tangential stresses and maintain jump in the normal stress (equivalent to the capillary pressure). This can be done by considering the velocity to be continuous across the interface, Γ:

$$\vec{u}_{\Gamma^-} = \vec{u}_{\Gamma^+} \tag{9}$$

The stress field must satisfy:

$$[-p\vec{I} + 2\mu\vec{E}]_\Gamma \cdot \vec{n} = \sigma\kappa\vec{n} \tag{10}$$

σ is the wetting/non-wetting fluid surface tension and $\vec{n}$ is the normal to the interface. The curvature κ is twice the mean curvature of the interface and is nominally the same as the one used in the level set method.

The above system of equations can be used to solve for the pressure and velocity fields for each of the two fluids. The condition set on the velocity and stress fields at the interface can be used to advect the interface. However, in a numerical implementation this would lead to solving for moving boundary conditions which is very complex and time-consuming, especially as we are dealing with two separate fluid domains [26]. To get around this problem, the VOF method was introduced by Hirt and Nichols in 1981 [24]. Essentially, instead of solving two sets of Navier-Stokes equations and keeping track of the fluid domain and shapes, we define an indicator function that identifies which fluid is contained in a given fluid cell.

If one considers a domain having two phases, wetting (P_w) and non-wetting (P_{nw}), then we can define an indicator function $I(\vec{x}, t)$,

$$I(\vec{x}, t) = \begin{cases} 1, & \vec{x} \in P_w \\ 0, & \vec{x} \in P_{nw} \end{cases}$$

For cells which are completely wetting phase, the liquid fraction is 1, while for non-wetting it is 0. The interface is located at $I = 1/2$, and is indicated by the Dirac delta function around the interface, $\delta_\Gamma = \delta(I - 1/2)$. We then get a modified form of the Navier-Stokes equation in the entire domain:

$$\frac{\partial\rho\vec{u}}{\partial t} + \nabla \cdot (\rho\vec{u}\vec{u}) = -\nabla \cdot p + \nabla \cdot (2\mu\vec{E}) + \vec{f_b} + \vec{f_s} \tag{11}$$

where we can write for the density and viscosity fields:

$$\begin{aligned} \rho(\vec{x}, t) &= \rho_w I(\vec{x}, t) + \rho_{nw}(1 - I(\vec{x}, t)) \\ \mu(\vec{x}, t) &= \mu_w I(\vec{x}, t) + \mu_{nw}(1 - I(\vec{x}, t)) \end{aligned} \tag{12}$$

The additional term introduced, $\vec{f_s}$ describes the Laplace pressure acting at the surface of discontinuity and is given by:

$$\vec{f_s} = \sigma\kappa\vec{n}\delta_\Gamma \tag{13}$$

For numerical implementation, the term $\vec{f_s}$ is replaced by a continuum surface force (CSF):

$$\vec{f_v} = \sigma\kappa\nabla I \tag{14}$$

$\vec{f_v}$ tends to $\vec{f_s}$ as the thickness of the interface region tends to zero. The curvature κ is calculated from the indicator function. It can be seen this is the same as the curvature in the level set method, where the indicator function replaces ϕ in Equation (4). Using mass conservation in combination with the modified Navier-Stokes equation (11), we finally get a simple advection equation for the indicator function:

$$\frac{\partial I}{\partial t} + \nabla \cdot (I\vec{u}) = 0 \tag{15}$$

To counterbalance numerical diffusion, a non-linear convective term is added to the equation, which acts as a shock that balances numerical diffusion.

$$\frac{\partial I}{\partial t} + \nabla \cdot (I\vec{u}) + \nabla \cdot (I(1-I)\vec{u_r}) = 0 \tag{16}$$

where $\vec{u}_r$ is a compression velocity. Its choice does not affect the solution outside the interfacial region. Note that the indicator function defines the interface implicitly as the 1/2 level set of I, and the advection equation for the indicator function is related to the level set equation (Equation (1)). An example smoothed indicator function is the Heaviside function, defined in Equation (3).

At the solid boundaries, the fluids are constrained in the pore space by requiring that the velocity component normal to the solid wall is zero. At the triple-contact line, Young's law determines the contact angle:

$$cos\theta = \frac{\sigma_{nw,s} - \sigma_{w,s}}{\sigma} \tag{17}$$

where $\sigma_{nw,s}$ is the non-wetting fluid/solid interfacial tension, $\sigma_{w,s}$ is the wetting fluid/solid interfacial tension.

For imposing the contact angle in our simulation, this is equivalent to imposing the boundary condition:

$$\vec{n}_{\Gamma_s} = \vec{n}_s cos\theta + \vec{t}_s sin\theta \tag{18}$$

where $\vec{t}_s$ is the unit tangential vector pointing into the wetting phase.

OpenFOAM uses finite volume discretization for the above equations for mass and momentum conservation, and advection of the indicator function. The advection equation (Equation (16)) is used to update the indicator function values throughout the domain. This is then used to update fluid properties throughout the domain, and calculate the surface force. Finally, the coupling between the pressure and velocity equation (Equation (11)) is performed by using the Pressure Implicit with Splitting of Operators (PISO) implicit pressure correction procedure. Further details on the implementation of interFoam and the numerical schemes used may be looked up in Deshpande *et al.* [48].

In order to calculate critical curvatures, we employ a quasi-static approach similar to the level set method presented earlier. We increase the pressure gradient in small steps, and allow the interface to reach equilibrium at each step. Since we are interested in only the equilibrium position, and the equilibrium arises from the balance of the pressure gradient and surface tension forces, we can arbitrarily choose the physical parameters of the system (chosen dimensionless and unitary here). For the same reason, we are allowed to arbitrarily add to the momentum equation extra damping (Darcy-like) terms. In fact, despite significantly changing the dynamics of the interface, this does not change the equilibrium position (being the additional term proportional to the velocity and, therefore vanishing at equilibrium). The advantage of this approach is that we can arbitrarily choose the Reynolds and capillary number to approach fast and smoothly the equilibrium position, while controlling the parasitic currents. Further details are shown in Appendix C. In addition, we use a special version of the interFoam solver, with local time stepping (LTSInterFoam), to march in pseudo-time with a pre-defined time step. This technique can maximize the time step (therefore reducing the relaxation time) in each cell. The resulting iterations are therefore not physical and not related to evolution in real time but simply represent internal iterations to reach the steady state. At each equilibrium step, thanks to the equilibrium of forces guaranteed by the Navier-Stokes equations, we get the equivalent curvature in the pore using the Young-Laplace equation, with the stationary Navier-Stokes solution for pressure at the two flow boundaries giving the capillary pressure, and the surface tension value imposed by us. All these choices make the VOF solver under study equivalent to the quasi-static level set formulation. The remaining differences lie in the different equations solved, in the implementation of curvature and the boundary conditions.

Since the finite-volume discretization is applicable both to structured

and unstructured grids[1], we tested the solver on two types of grids: a regular Cartesian grid (the same one used for the level set method) and a grid locally adapted to the interface. In both cases the mesh generator snappyHexMesh has been used to automatically generate the mesh from analytical information on the sphere geometry. Preliminary results show no significant differences for the mean curvature measured. This is due to the fact that no explicit geometrical information about the interface is used by the solver. The curvature and surface tension discretization is totally done based on the concentration field. Therefore the shape of the cell close to the interface is not very important when there is no flow occurring. For this reason in the following results, only the simulations with the regular Cartesian grids are presented.

2.3. Analytical and experimental observations

Mason and Morrow [33] published a semi-analytical calculation of the maximum curvatures (also called critical curvatures) for the rhomboidal pore for a range of contact angles and rhomboid pore angles, and experimentally validated their results. In this work we compare our simulation results against their semi-analytical values.

We briefly provide their methodology followed by them in Appendix B. Further details may be obtained in their original work. For completeness, we also provide their calculations in Appendix A.

[1]OpenFOAM however always uses an unstructured indexing of the mesh, therefore no significant speed-up is obtained when using structured grid. As a general note, unstructured meshes can better capture the complex curved shape of walls but the accuracy of the numerical discretization schemes can however deteriorate for highly distorted unstructured grids.

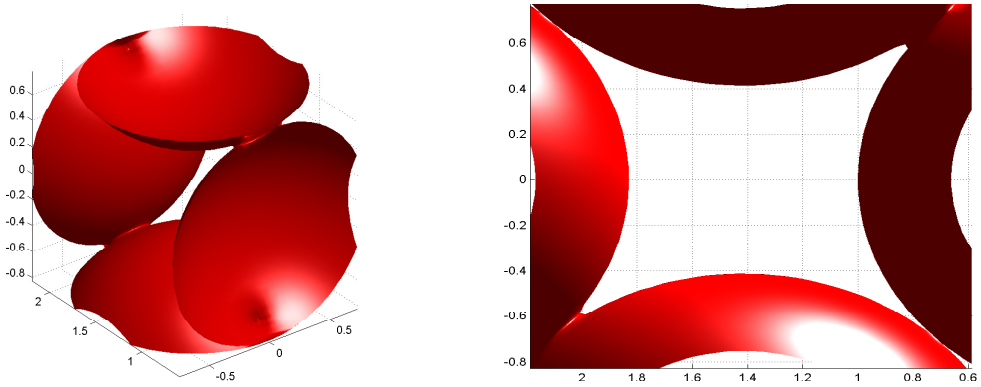

(a) Default view of 3D pore throat. (b) Cross section of flow.

Figure 2: 3D pore throat geometry for rhomboid angle 45°.

3. Results and Discussion

The results from the quasi-static level set and the Navier-Stokes volume-of-fluid (OpenFOAM) solvers are compared with those obtained by Mason and Morrow [33] for the actual pore throat geometries, like the one in Fig. 2. The semi-analytical results are summarized in Table A.1. Values obtained from both codes are also listed in the Appendix, in Tables A.2 and A.4. The maximum mean curvature computation results for each contact angle are shown in Figure 5. Errors for each case are reported in Tables A.3 and A.5. The values and errors for running the level set method without the overlap are presented in Tables A.6 and A.7, respectively.

Prior to performing simulations on 3D pore geometries for the level set formulation, the technique was first tested on 2D geometries. The results for those are available in [49]. The simulation results presented here follow the analytical cases for which Mason and Morrow [33] determined maximum mean curvatures. The rhomboid half-angles vary from 31° to 45°. Representative geometry is shown for rhomboid half-angle of 45° in Figure 2. For each rhomboid half-angle, contact angle varied from 0° to 90°. Errors for each case are reported in Table A.3.

In the following figures, the solid walls are shown in transparent color while the fluid interface is shown in red. The reconstruction of the interface at equilibrium, with both codes, for rhomboid angles 45° and 31° and contact angles 10° and 80° is reported in Figures 3 and 4. The dimensions of the domain and the size of the mesh spacing are the same; however, since data are stored in a different format, the figures may look slightly different

due to different visualization algorithm. These cases represent extremities in contact angle as well as rhomboid half-angle and are hence good for showcasing the method's accuracy. MS-P theory predicts a divided meniscus for rhomboid half-angle 31°. As can be seen in Figure 4, this is effectively captured in the simulations.

For performing the simulations with zero contact angle in the level set method, we follow the recommendations of Jettestuen *et al.* [14] and use the original LSMPQS software [50]. That code is in C/FORTRAN, and is also otherwise faster than the modified method due to its simplicity. We obtain an excellent match with the analytical solution. The OpenFOAM results are also very good for this case. The grid spacing used here is 0.02. Note that the disk/sphere radii in all examples is 1, and the reported grid spacing and all lengths are relative to the radii. For the other cases (with contact angle larger than zero) with the level set method, we used a slightly different (MATLAB-based) implementation, and due to higher computational costs, the grid spacing was set to 0.04. For consistency, the OpenFOAM results shown in Figure 5 were also run with the same grid size of 0.04. A grid convergence study was also performed for OpenFOAM, by making the grid twice as fine (grid size 0.02). The results did not show significant improvement. We present those results in the Appendix C. The results shown in Figure 5 show both methods performing well for lower contact angles, while the OpenFOAM solver has higher errors for high contact angles. In some cases, the level set method seems to overshoot the analytical predictions for high rhomboid angles. This is likely an artifact of the numerical overlap imposed. As described in the previous section, the overlap between the pore space and rock was used to ensure proper formation of the contact angle in the level set method. The overlap is going to present problems when simulating larger samples with narrow solid regions as discussed in Jettestuen *et al.* [14]. The adaptive meshing schemes that will address the problem will be investigated in future work. The OpenFOAM boundary conditions did not require an overlap.

Another important aspect is the initial condition. A starting curvature that allows the interface to find a stable position within the pore space in general geometries is not known *a priori* which prompted the development of the compressible model in [16]. In this work with simple pore throats, we did not find it necessary to run the compressible model. It was enough to guess a sensible starting value of the normal velocity term for all cases. We choose a starting value of 0.15 for the normal velocity term κ_0 and allow the interface to find the equilibrium position (steady state solution to Equation (2)). For the OpenFOAM simulations, the relaxation to equilibrium is

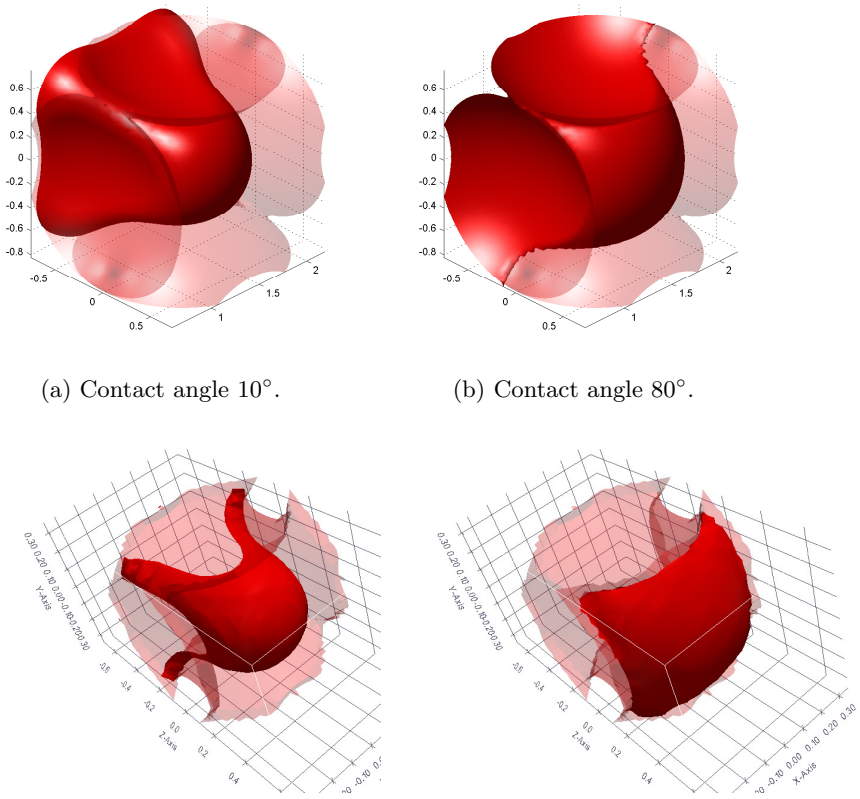

(a) Contact angle 10°.

(b) Contact angle 80°.

(c) Contact angle 10°.

(d) Contact angle 80°.

Figure 3: Interfaces at the critical value of curvature for the pore throat with rhomboid angle 45° for two extreme cases of contact angle, showing comparison between level set (top - NW phase in red), and OpenFOAM (bottom - fluid/fluid interface in red). After the critical value, the pore throat is drained and we do not observe main meniscus within it any more. Solid surfaces are shown as transparent.

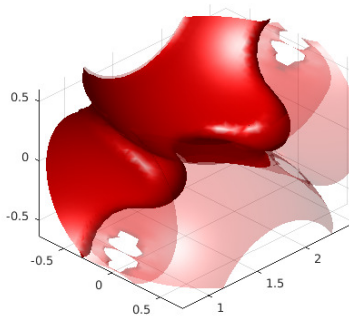

(a) Contact angle 10°.

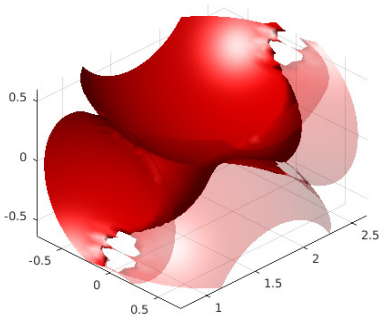

(b) Contact angle 80°.

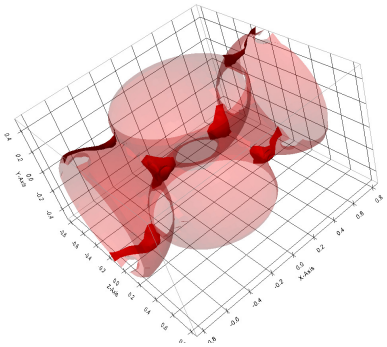

(c) Contact angle 10°.

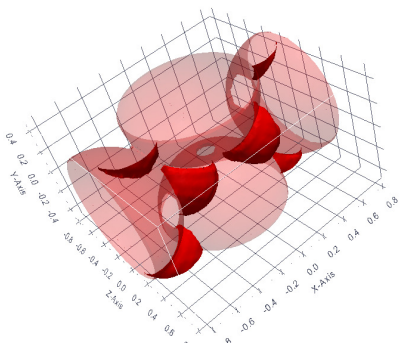

(d) Contact angle 80°.

Figure 4: Critical curvature interfaces (in red) for rhomboid angle 31°: comparison between level set (top - NW phase in red) and OpenFOAM (bottom - fluid/fluid interface in red) for two extreme cases of contact angle. The figures show divided meniscus, in agreement with MS-P theory.

solely driven by the imposed pressure drops at the boundaries and, for these particular converging-diverging pores, every initial interface position gives the same final equilibrium result. However, to speed up the computations, the interface has always been placed in the middle of the domain and the initial pressure drop set to a fraction (typically 0.8) of the reference analytical results. As already mentioned in the previous section, the pressure drop is then increased until the interface reaches its maximum curvature position before being transported out of the domain when the imposed pressure becomes larger than the pore entry capillary pressure. We demonstrate improvements in convergence to equilibrium due to the damping term for two extreme cases in figures C.12 and C.13 in Appendix C. The figures compare changes in saturation and velocity at each capillary pressure step, with and without the damping term. At each capillary pressure step, there is a sharp jump in both velocities and saturations. As the system moves to equilibrium, this dies out. Without the damping term, the jumps are more extreme. This clearly shows the advantage of using the damping term, as we achieve the same equlibrium condition faster.

A pertinent point on the actual calculation of the curvatures is that for the level set method, we use the formulation proposed by Osher and Sethian [22] in their original work (see Equation (4)). The level set code incorporates that by calculating the curvatures at every grid point up to second order accuracy. The difficulty here is that the actual interface passes in between grid points, causing significant differences in accuracy of the method if one chooses to take the nearest grid point for calculating curvatures instead of the actual interface. Hence, we first found the exact interface coordinates, and then interpolated the curvatures given at the grid points to find the curvatures on all the points of the interface. The curvatures reported in Table A.2 are the mean values of the curvatures from all the points on the interface. Taking the mean value for the curvature is problematic in some of the simulation cases as there is a wide spread in curvature values at different points of the interface.

We exemplify this for contact angles 10° and 90°, and rhomboid half-angles 31° and 45° in Figure 6. For the first case (rhomboid angle 31°), we can see that the spread in values is quite high due to tight pore spaces where solid surfaces are too close together and resolution should be finer. This results in a high error when we compare the calculated mean curvature with analytical values. Additionally, for the worst case of contact angle 90°, the change in curvature values near the boundaries is much sharper, but the diffusive nature of the level set method ensures a smooth interface. For the second case (rhomboid angle 45°), we can see that the interface is

much better resolved, and we get a lower final error, though in this case also, a contact angle of 90° results in sharp changes in curvature near the boundaries. The case for contact angle 90° has the highest errors, up to 25%. This case is like a piston moving across the pore, and this causes large intersection regions between solid and non-wetting fluid phase. However, even in this extreme contact angle, most of the cases have errors in the range of 10%. This also highlights the importance of adaptive meshing for imposition of contact angles. Near the solid-liquid-liquid contact line at the boundary, we can have a much finer grid, with coarser grid cells in the main pore space. So we can better capture the contact angle at the boundary, with lesser computational expense. The curvatures are more difficult to resolve in the same areas. Note that, for the level set method, we already tried higher order accurate numerical schemes without much improvement. For OpenFOAM, higher order accurate schemes for general unstructured meshes are not available. Finer grid cells near the boundary however can be added. Thus, adaptive meshing seems a logical course to follow for future work on these methods. This will surely have a beneficial effect in the local computations of curvatures. Whether this has an effect on more general displacement problems is something that requires more studies. The OpenFOAM results, in fact, suggest that a grid refinement is not improving the overall capillary pressure estimated by the balance of forces solved in the momentum equation. This mean that other factors (e.g. the way the contact angle is imposed) might be important.

The overall results show promise for more general applications. Imaging has the potential of informing us of the distribution of wettability on a given rock sample by identification of the mineralogy and possible bitumen coatings [51]. In that case, we could map surfaces of different wettability and a method which can predict the behavior of capillary-dominated flow in a given rock sample can be applicable. Jettestuen *et al.* [14] have shown the method applied to simple mixed wet systems. However, it is likely that more general porous media geometries would be more problematic. If one were to attempt simulating flow in an image from a rock sample, the error margins would likely be larger and a relatively small error (like the ones observed here) might propagate to the macro-scale in a unpredictable way. Our future work will also benchmark with other methods (such as the lattice Boltzmann method) to increase awareness of potential limitations and to provide better accuracy assessment of the methods.

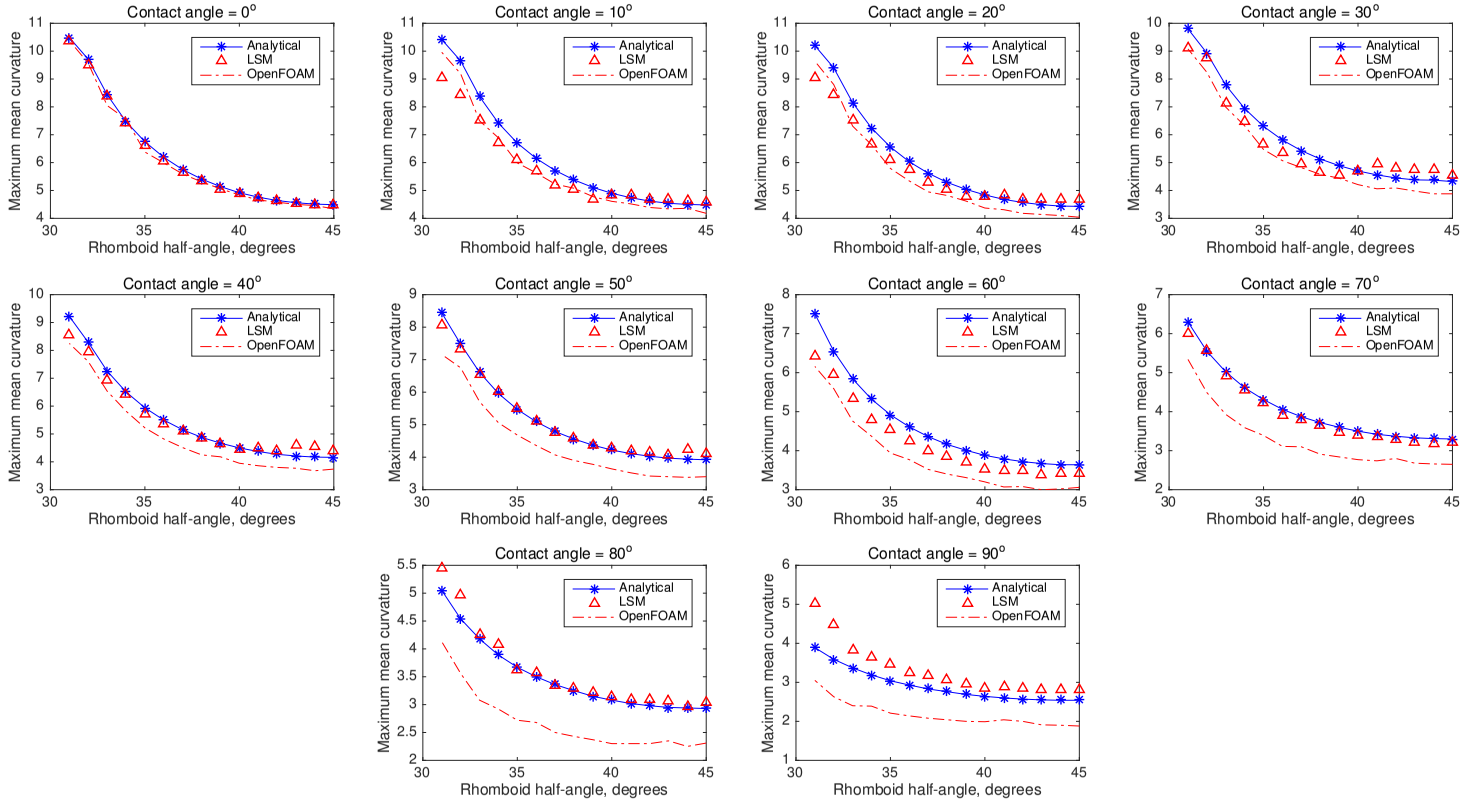

Figure 5: Maximum mean curvature as a function of rhomboid half-angles for different contact angles: Analytical vs. numerical values.

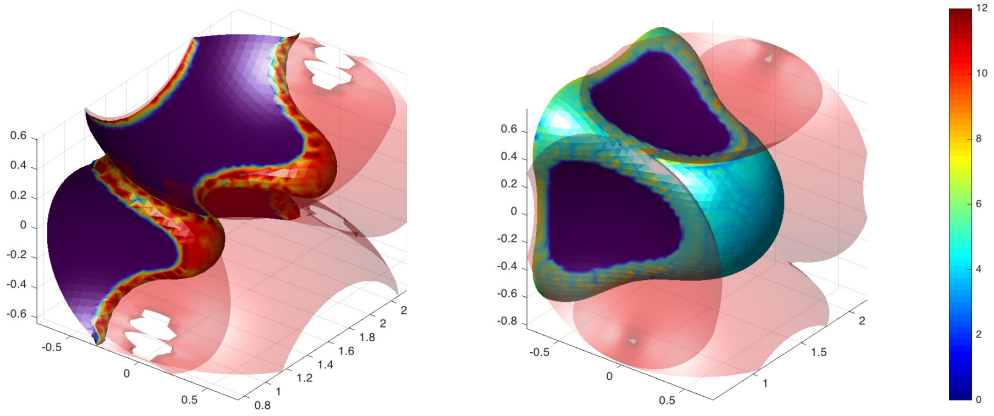

(a) Rhomboid angle= 31°, $\theta = 10°$ (b) Rhomboid angle= 45°, $\theta = 10°$

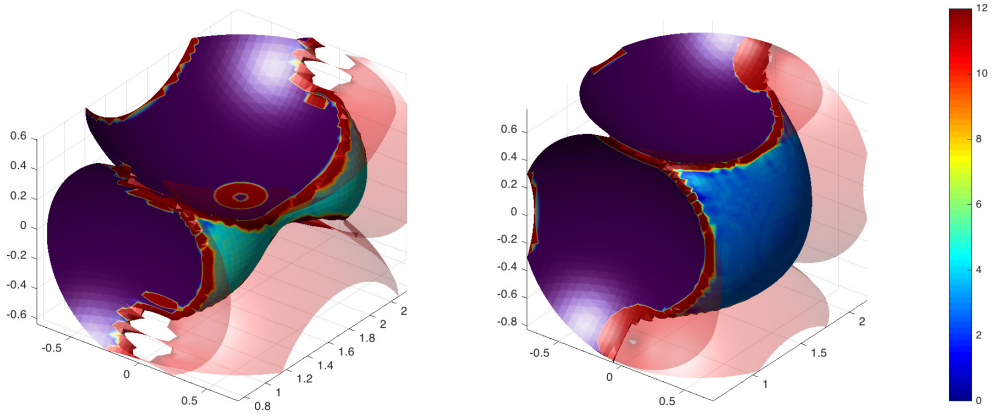

(c) Rhomboid angle= 31°, $\theta = 90°$ (d) Rhomboid angle= 45°, $\theta = 90°$

Figure 6: Curvature distribution for rhomboid angles 31° and 45°, for contact angle 10° and 90°, for the level set simulations.

4. Conclusion

We have quantified the accuracy of two popular methods for capillarity dominated quasi-static displacements in a set of converging-diverging pore throat geometries, namely a level set method and an algebraic volume of fluid (within the OpenFOAM software). Both methods perform well for lower contact angles, though we observed better accuracy for the level set method for contact angles more than 70°, while both methods struggle with 90° contact angle. For other problems where viscosity (or gravity) plays a more dominant role certainly Navier-Stokes based solvers such as OpenFOAM are more appropriate, and this version of the level set method should not be used.

Validation of numerical methods is most commonly done in constant cross-section geometries since that is where analytical solutions exist. Similar is true for widely accepted lattice Boltzmann methods. There is a gap between testing in tubes [32] and simulation in larger geometries [43]. The only way to test larger geometries is against experiments, which are not always available.

This kind of validation is particularly important in larger geometries, where it if often required to sacrifice some accuracy for much lower computational time. One also may choose to use a lower precision numerical scheme (like first order accuracy in time) to get results faster. The presented implementation of the level set method has not been optimized for running large cases. In future work, an optimized code will be used to study larger geometries as well as real rock images, where convergence criteria could be relaxed a little for much lower computational time. Determining when the simulation has converged is usually the judgment of the individual user. Hence, as direct pore scale modeling approaches become more popular, validation against other codes and experimental results will be crucial to check the overall reliability of the results.

We expect that these kind of validation studies will also become increasingly important in other problems such as imbibition in porous media, where most larger-scale models fail. Imbibition is more difficult to model with quasi-static approaches than drainage. In the future we will quantify the differences between quasi-static and dynamic approaches in imbibition: while most of imbibition studies have been done using quasi-static approaches due to computational complexity, it remains an open question if they are adequate in describing ultimate fluid configuration (and also relative permeability).

5. Acknowledgements

This work was supported by the Gas EOR consortium at UT Austin (RV), by NSF CAREER grant 1255622 (MP) and by the King Abdullah University of Science and Technology (KAUST) (MI). MI was supported by the Academic Excellency Alliance (AEA) UT Austin-KAUST project "Uncertainty quantification for predictive modeling of the dissolution of porous and fractured media" and by the KAUST SRI Center for Uncertainty Quantification in Computational Science and Engineering.

6. References

[1] N. Morrow, Wettability and its effect on oil recovery, Journal of Petroleum Technology 42 (12). doi:10.2118/21621-PA.

[2] N. Morrow, H. Lim, J. Ward, Effect of crude-oil-induced wettability changes on oil recovery, SPE Formation Evaluation 1 (1). doi:10.2118/13215-PA.

[3] C. H. Pentland, R. El-Maghraby, S. Iglauer, M. J. Blunt, Measurements of the capillary trapping of super-critical carbon dioxide in berea sandstone, Geophysical Research Letters 38 (6).

[4] S. Iglauer, A. Paluszny, C. H. Pentland, M. J. Blunt, Residual CO2 imaged with X-ray micro-tomography, Geophysical Research Letters 38 (21).

[5] M. J. Blunt, B. Bijeljic, H. Dong, O. Gharbi, S. Iglauer, P. Mostaghimi, A. Paluszny, C. Pentland, Pore-scale imaging and modelling, Advances in Water Resources 51 (2013) 197–216. doi:10.1016/j.advwatres.2012.03.003.

[6] Y.-S. Wu, B. Bai, et al., Efficient simulation for low salinity waterflooding in porous and fractured reservoirs, in: SPE Reservoir Simulation Symposium, Society of Petroleum Engineers, 2009.

[7] M. Cil, J. C. Reis, M. A. Miller, D. Misra, et al., An examination of countercurrent capillary imbibition recovery from single matrix blocks and recovery predictions by analytical matrix/fracture transfer functions, in: SPE Annual Technical Conference and Exhibition, Society of Petroleum Engineers, 1998.

[8] A. Gupta, F. Civan, et al., An improved model for laboratory measurement of matrix to fracture transfer function parameters in immiscible displacement, in: SPE Annual Technical Conference and Exhibition, Society of Petroleum Engineers, 1994.

[9] D. Wildenschild, A. P. Sheppard, X-ray imaging and analysis techniques for quantifying pore-scale structure and processes in subsurface porous medium systems, Advances in Water Resources 51 (2013) 217–246.

[10] P. Meakin, A. M. Tartakovsky, Modeling and simulation of pore-scale multiphase fluid flow and reactive transport in fractured

and porous media, Reviews of Geophysics 47 (3) (2009) n/a–n/a. doi:10.1029/2008RG000263.

[11] M. J. Blunt, M. D. Jackson, M. Piri, P. H. Valvatne, Detailed physics, predictive capabilities and macroscopic consequences for pore-network models of multiphase flow, Advances in Water Resources 25 (8–12) (2002) 1069–1089. doi:10.1016/S0309-1708(02)00049-0.

[12] T. J. Baker, Mesh generation: Art or science?, Progress in Aerospace Sciences 41 (1) (2005) 29–63.

[13] M. Icardi, G. Boccardo, R. Tempone, On the predictivity of pore-scale simulations: Estimating uncertainties with multilevel monte carlo, Advances in Water Resources 95 (2016) 46–60.

[14] E. Jettestuen, J. O. Helland, M. Prodanović, A level set method for simulating capillary-controlled displacements at the pore scale with nonzero contact angles, Water Resources Research 49 (8) (2013) 4645–4661. doi:10.1002/wrcr.20334.

[15] S. Osher, J. A. Sethian, Fronts propagating with curvature-dependent speed: Algorithms based on Hamilton-Jacobi formulations, Journal of Computational Physics 79 (1) (1988) 12–49. doi:10.1016/0021-9991(88)90002-2.

[16] M. Prodanović, S. L. Bryant, A level set method for determining critical curvatures for drainage and imbibition, Journal of Colloid and Interface Science 304 (2) (2006) 442–458. doi:10.1016/j.jcis.2006.08.048.

[17] S. O. Unverdi, G. Tryggvason, A front-tracking method for viscous, incompressible, multi-fluid flows, Journal of computational physics 100 (1) (1992) 25–37.

[18] E. Olsson, G. Kreiss, A conservative level set method for two phase flow, Journal of Computational Physics 210 (1) (2005) 225–246. doi:10.1016/j.jcp.2005.04.007.

[19] H.-K. Zhao, B. Merriman, S. Osher, L. Wang, Capturing the behavior of bubbles and drops using the variational level set approach, Journal of Computational Physics 143 (2) (1998) 495–518. doi:10.1006/jcph.1997.5810.

[20] S. Esodoglu, P. Smereka, A variational formulation for a level set representation of multiphase flow and area preserving curvature flow, Communications in Mathematical Sciences 6 (1) (2008) 125–148, mathematical Reviews number (MathSciNet): MR2398000; Zentralblatt MATH identifier: 1137.76067.

[21] D. Enright, R. Fedkiw, J. Ferziger, I. Mitchell, A hybrid particle level set method for improved interface capturing, Journal of Computational physics 183 (1) (2002) 83–116.

[22] S. Osher, R. Fedkiw, Level Set Methods and Dynamic Implicit Surfaces, Springer, 2003.

[23] J. A. Sethian, Level Set Methods and Fast Marching Methods: Evolving Interfaces in Computational Geometry, Fluid Mechanics, Computer Vision, and Materials Science, Cambridge University Press, 1999.

[24] C. W. Hirt, B. D. Nichols, Volume of fluid (vof) method for the dynamics of free boundaries, Journal of computational physics 39 (1) (1981) 201–225.

[25] A. Ferrari, I. Lunati, Direct numerical simulations of interface dynamics to link capillary pressure and total surface energy, Advances in Water Resources 57 (2013) 19–31.

[26] A. Ferrari, I. Lunati, Inertial effects during irreversible meniscus reconfiguration in angular pores, Advances in Water Resources 74 (2014) 1–13.

[27] D. A. Hoang, V. van Steijn, L. M. Portela, M. T. Kreutzer, C. R. Kleijn, Benchmark numerical simulations of segmented two-phase flows in microchannels using the volume of fluid method, Computers & Fluids 86 (2013) 28–36.

[28] P. Horgue, F. Augier, P. Duru, M. Prat, M. Quintard, Experimental and numerical study of two-phase flows in arrays of cylinders, Chemical Engineering Science 102 (2013) 335–345.

[29] A. Q. Raeini, M. J. Blunt, B. Bijeljic, Modelling two-phase flow in porous media at the pore scale using the volume-of-fluid method, Journal of Computational Physics 231 (17) (2012) 5653–5668.

[30] M. Sussman, P. Smereka, S. Osher, A level set approach for computing solutions to incompressible two-phase flow, Journal of Computational Physics 114 (1) (1994) 146–159. doi:10.1006/jcph.1994.1155.

[31] D. Gerlach, G. Tomar, G. Biswas, F. Durst, Comparison of volume-of-fluid methods for surface tension-dominant two-phase flows, International Journal of Heat and Mass Transfer 49 (34) (2006) 740–754. doi:10.1016/j.ijheatmasstransfer.2005.07.045.
URL http://www.sciencedirect.com/science/article/pii/S0017931005005314

[32] H. S. Rabbani, V. Joekar-Niasar, N. Shokri, Effects of intermediate wettability on entry capillary pressure in angular pores, Journal of Colloid and Interface Science 473. doi:10.1016/j.jcis.2016.03.053.
URL http://www.sciencedirect.com/science/article/pii/S0021979716301953

[33] G. Mason, N. R. Morrow, Effect of contact angle on capillary displacement curvatures in pore throats formed by spheres, Journal of Colloid and Interface Science 168 (1) (1994) 130–141. doi:10.1006/jcis.1994.1402.

[34] M. A. Celia, P. C. Reeves, L. A. Ferrand, Recent advances in pore scale models for multiphase flow in porous media, Reviews of Geophysics 33 (S2) (1995) 1049–1057. doi:10.1029/95RG00248.

[35] D. Wildenschild, C. Vaz, M. Rivers, D. Rikard, B. Christensen, Using X-ray computed tomography in hydrology: systems, resolutions, and limitations, Journal of Hydrology 267 (3) (2002) 285–297.

[36] G. M. Homsy, Viscous fingering in porous media, Annual Review of Fluid Mechanics 19 (1) (1987) 271–311.

[37] D. B. Ingham, I. Pop, Transport phenomena in porous media III, Vol. 3, Elsevier, 2005.

[38] M. T. Van Genuchten, P. Wierenga, Mass transfer studies in sorbing porous media I. analytical solutions, Soil Science Society of America Journal 40 (4) (1976) 473–480.

[39] M. Khishvand, A. Alizadeh, M. Piri, In-situ characterization of wettability and pore-scale displacements during two-and three-phase flow in natural porous media, Advances in Water Resources 97 (2016) 279–298.

[40] M. Andrew, B. Bijeljic, M. J. Blunt, Pore-scale contact angle measurements at reservoir conditions using x-ray microtomography, Advances in Water Resources 68 (2014) 24–31.

[41] M. Andrew, H. Menke, M. J. Blunt, B. Bijeljic, The imaging of dynamic multiphase fluid flow using synchrotron-based x-ray microtomography at reservoir conditions, Transport in Porous Media 110 (1) (2015) 1–24.

[42] C. J. Landry, Z. T. Karpyn, O. Ayala, Pore-Scale Lattice Boltzmann Modeling and 4d X-ray Computed Microtomography Imaging of Fracture-Matrix Fluid Transfer, Transport in Porous Media 103 (3) (2014) 449–468. doi:10.1007/s11242-014-0311-x.
URL https://link.springer.com/article/10.1007/s11242-014-0311-x

[43] C. J. Landry, Z. T. Karpyn, O. Ayala, Relative permeability of homogenous-wet and mixed-wet porous media as determined by pore-scale lattice Boltzmann modeling, Water Resources Research 50 (5) (2014) 3672–3689. doi:10.1002/2013WR015148.
URL http://onlinelibrary.wiley.com/doi/10.1002/2013WR015148/abstract

[44] H. Huang, D. T. Thorne, M. G. Schaap, M. C. Sukop, Proposed approximation for contact angles in Shan-and-Chen-type multicomponent multiphase lattice Boltzmann models, Physical Review E 76 (6) (2007) 066701. doi:10.1103/PhysRevE.76.066701.
URL http://link.aps.org/doi/10.1103/PhysRevE.76.066701

[45] M. Prodanović, W. Lindquist, R. Seright, Porous structure and fluid partitioning in polyethylene cores from 3d X-ray microtomographic imaging, Journal of Colloid and Interface Science 298 (1) (2006) 282–297. doi:10.1016/j.jcis.2005.11.053.

[46] I. M. Mitchell, A toolbox of level set methods, Dept. Comput. Sci., Univ. British Columbia, Vancouver, BC, Canada, http://www. cs. ubc. ca/˜ mitchell/ToolboxLS/, Tech. Rep. TR-2004-09.

[47] I. M. Mitchell, The flexible, extensible and efficient toolbox of level set methods, Journal of Scientific Computing 35 (2-3) (2008) 300–329.

[48] S. S. Deshpande, L. Anumolu, M. F. Trujillo, Evaluating the performance of the two-phase flow solver interfoam, Computational science & discovery 5 (1) (2012) 014016.

[49] R. Verma, Validation of level set contact angle method for multiphase flow in porous media, Master's thesis, University of Texas at Austin (2014).

[50] M. Prodanović, Level set method based progressive quasi-static (LSM-PQS) software, http://users.ices.utexas.edu/ masha/lsmpqs/.

[51] L. Crandell, C. A. Peters, W. Um, K. W. Jones, W. B. Lindquist, Changes in the pore network structure of hanford sediment after reaction with caustic tank wastes, Journal of contaminant hydrology 131 (1) (2012) 89–99.

[52] W. Purcell, et al., Interpretation of capillary pressure data, Journal of Petroleum Technology 2 (08) (1950) 11–12.

[53] G. Mason, N. Morrow, Meniscus displacement curvatures of a perfectly wetting liquid in capillary pore throats formed by spheres, Journal of colloid and interface science 109 (1) (1986) 46–56.

Appendix A. Tables for analytical and calculated values

In this section, critical curvature values obtained by Mason and Morrow [33] are presented, alongwith the values obtained from the level set method, and the OpenFOAM VOF method. We also present the errors for each case of the numerical methods, with respect to Mason and Morrow's values. The cases where errors are larger than 25% are in bold, while cases with errors between 15-25% are italicized.

Table A.1: Critical curvature values calculated by Mason and Morrow [33].

	Contact angle θ in degrees									
Rhomboid half-angle	0	10	20	30	40	50	60	70	80	90
45	4.49	4.48	4.43	4.32	4.16	3.92	3.64	3.30	2.93	2.54
44	4.51	4.50	4.44	4.37	4.17	3.94	3.64	3.31	2.94	2.54
43	4.56	4.54	4.49	4.38	4.21	3.97	3.67	3.33	2.95	2.55
42	4.64	4.62	4.57	4.45	4.27	4.03	3.72	3.37	2.98	2.57
41	4.76	4.74	4.68	4.56	4.37	4.11	3.79	3.42	3.02	2.60
40	4.92	4.90	4.84	4.70	4.50	4.22	3.88	3.50	3.08	2.64
39	5.14	5.11	5.04	4.89	4.67	4.37	4.01	3.60	3.15	2.69
38	5.41	5.38	5.29	5.13	4.88	4.56	4.16	3.72	3.25	2.76
37	5.75	5.72	5.62	5.43	5.15	4.79	4.36	3.87	3.36	2.83
36	6.19	6.15	6.03	5.81	5.50	5.09	4.61	4.06	3.50	2.93
35	6.75	6.70	6.56	6.30	5.94	5.47	4.92	4.31	3.67	3.04
34	7.47	7.42	7.24	6.94	6.51	5.96	5.32	4.61	3.89	3.19
33	8.44	8.37	8.15	7.78	7.26	6.61	5.84	5.02	4.18	3.37
32	9.71	9.65	9.40	8.93	8.29	7.48	6.55	5.55	4.54	3.59
31	10.49	10.42	10.20	9.80	9.22	8.44	7.51	6.30	5.05	3.89

Table A.2: Critical curvature values calculated from the level set method.

	Contact angle θ in degrees									
Rhombus half-angle	0	10	20	30	40	50	60	70	80	90
45	4.49	4.58	4.67	4.53	4.4	4.1	3.43	3.23	3.05	2.81
44	4.5	4.64	4.7	4.76	4.55	4.22	3.43	3.19	2.97	2.81
43	4.54	4.69	4.69	4.75	4.58	4.06	3.38	3.23	3.06	2.8
42	4.63	4.67	4.68	4.81	4.37	4.17	3.48	3.27	3.08	2.84
41	4.72	4.83	4.85	4.94	4.49	4.19	3.5	3.36	3.1	2.89
40	4.87	4.82	4.79	4.68	4.47	4.3	3.53	3.38	3.13	2.83
39	5.05	4.69	4.77	4.53	4.63	4.39	3.71	3.46	3.21	2.97
38	5.32	5.04	5.02	4.65	4.83	4.59	3.84	3.65	3.3	3.05
37	5.65	5.21	5.28	4.97	5.08	4.77	3.98	3.79	3.35	3.19
36	6.05	5.72	5.76	5.36	5.38	5.09	4.25	3.89	3.56	3.25
35	6.63	6.11	6.13	5.65	5.72	5.51	4.55	4.22	3.63	3.47
34	7.4	6.72	6.68	6.49	6.4	6	4.81	4.57	4.08	3.64
33	8.41	7.5	7.52	7.15	6.91	6.56	5.33	4.9	4.25	3.83
32	9.5	8.43	8.44	8.75	7.95	7.33	5.97	5.57	4.96	**4.49**
31	10.39	9.04	9.04	9.13	8.57	8.06	6.44	6.01	5.46	**5.01**

Table A.3: Relative errors for each case for level set method, in %.

	Contact angle θ, in degrees									
Rhombus half-angle	0	10	20	30	40	50	60	70	80	90
45	0.00	-2.23	-5.42	-4.86	-5.77	-4.59	5.77	2.12	-4.10	-10.63
44	0.22	-3.11	-5.86	-8.89	-9.11	-7.11	5.77	3.63	-1.02	-10.63
43	0.44	-3.30	-4.45	-8.45	-8.79	-2.27	7.90	3.00	-3.73	-9.8
42	0.22	-1.08	-2.41	-8.05	-2.34	-3.47	6.45	2.97	-3.36	-10.51
41	0.84	-1.90	-3.63	-8.26	-2.75	-1.95	7.65	1.75	-2.65	-11.15
40	1.02	1.63	1.03	0.43	0.67	-1.90	9.02	3.43	-1.62	-7.02
39	1.75	8.22	5.36	7.36	0.86	-0.46	7.48	3.89	-1.90	-10.41
38	1.66	6.32	5.10	9.36	1.02	-0.66	7.69	1.88	-1.54	-10.51
37	1.74	8.92	6.05	8.47	1.36	0.42	8.72	2.07	0.30	-12.72
36	2.26	6.99	4.48	7.75	2.18	0.00	7.81	4.19	-1.71	-10.92
35	1.78	8.81	6.55	10.32	3.70	-0.73	7.52	2.09	1.09	-14.14
34	0.94	9.43	7.73	6.48	1.69	-0.67	9.59	0.87	-4.88	-14.11
33	0.36	10.39	7.73	8.10	4.82	0.76	8.73	2.39	-1.67	-13.65
32	2.16	12.64	10.21	2.02	4.10	2.01	8.85	-0.36	-9.25	**-25.07**
31	0.95	13.24	11.37	6.84	7.05	4.50	14.22	4.60	-8.12	**-28.79**

Table A.4: Critical curvature values calculated from the OpenFOAM VOF method.

	Contact angle θ in degrees									
Rhombus half-angle	0	10	20	30	40	50	60	70	80	90
45	4.34	4.18	4.04	3.88	3.74	3.40	*3.06*	*2.65*	*2.31*	**1.88**
44	4.46	4.36	4.10	3.88	3.68	3.38	*3.02*	*2.66*	*2.25*	**1.90**
43	4.50	4.34	4.14	3.98	3.77	3.40	*3.00*	*2.68*	*2.35*	**1.91**
42	4.58	4.39	4.18	4.09	3.80	*3.42*	*3.08*	*2.80*	*2.30*	*2.00*
41	4.66	4.52	4.31	4.06	3.86	3.52	*3.07*	*2.74*	*2.30*	*2.04*
40	4.84	4.61	4.37	4.21	3.95	3.64	*3.20*	*2.77*	**2.30**	*1.99*
39	5.06	4.78	4.62	4.44	4.18	3.78	*3.31*	*2.84*	*2.37*	**2.00**
38	5.31	5.08	4.82	4.58	4.25	3.90	*3.40*	*2.91*	**2.43**	**2.04**
37	5.59	5.23	4.95	4.82	4.51	*4.07*	*3.52*	*3.10*	**2.50**	**2.08**
36	5.99	5.63	5.34	5.07	4.82	4.36	*3.77*	*3.11*	*2.68*	**2.14**
35	6.38	5.99	5.79	5.47	5.22	4.68	*3.94*	*3.39*	**2.72**	**2.21**
34	7.56	6.89	6.64	6.32	5.82	*5.06*	*4.37*	*3.59*	*2.92*	**2.39**
33	8.05	7.50	7.31	6.99	6.54	5.71	*4.76*	*3.93*	**3.08**	**2.40**
32	9.57	9.19	8.80	8.24	7.60	6.75	5.59	*4.49*	*3.56*	**2.63**
31	10.38	9.96	9.64	9.08	8.25	*7.16*	*6.16*	*5.34*	*4.13*	*3.05*

Table A.5: Relative errors for each case for OpenFOAM VOF method, in %.

	Contact angle θ in degrees									
Rhombus half-angle	0	10	20	30	40	50	60	70	80	90
45	3.34	6.70	8.80	10.19	10.10	13.27	*15.93*	*19.70*	*21.16*	**25.98**
44	1.11	3.11	7.66	11.21	11.75	14.21	*17.03*	*19.64*	*23.47*	**25.20**
43	1.32	4.41	7.80	9.13	10.45	14.36	*18.26*	*19.52*	*20.34*	**25.10**
42	1.29	4.98	8.53	8.09	11.01	*15.14*	*17.20*	*16.91*	*22.82*	*22.18*
41	2.10	4.64	7.91	10.96	11.67	14.36	*19.00*	*19.88*	*23.84*	*21.54*
40	1.63	5.92	9.71	10.43	12.22	13.74	*17.53*	*20.86*	**25.32**	*24.62*
39	1.56	6.46	8.33	9.20	10.49	13.50	*17.46*	*21.11*	*24.76*	**25.65**
38	1.85	5.58	8.88	10.72	12.91	14.47	*18.27*	*21.77*	**25.23**	**26.09**
37	2.78	8.57	11.92	11.23	12.43	*15.03*	*19.27*	*19.90*	**25.60**	**26.50**
36	3.23	8.46	11.44	12.74	12.36	14.34	*18.22*	*23.40*	*23.43*	**26.96**
35	5.48	10.60	11.74	13.17	12.12	14.44	*19.92*	*21.35*	**25.89**	**27.30**
34	-1.20	7.14	8.29	8.93	10.60	*15.10*	*17.86*	*22.13*	*24.94*	**25.08**
33	4.62	10.39	10.31	10.15	9.92	13.62	*18.49*	*21.71*	**26.32**	**28.78**
32	1.44	4.77	6.38	7.73	8.32	9.76	14.66	*19.10*	*21.59*	**26.74**
31	1.05	4.41	5.49	7.35	10.52	*15.17*	*17.98*	*15.24*	*18.22*	*21.59*

Table A.6: Level set values for five cases with no overlap

	Contact angle				
Rhomboid half-angle	50	60	70	80	90
45	4.80	4.86	4.86	4.88	4.94
44	4.78	4.83	4.85	4.91	4.91
43	4.87	4.93	4.93	5.00	5.00
42	4.94	4.97	5.00	5.01	5.06
41	5.07	5.13	5.13	5.16	5.21
40	5.03	5.10	5.10	5.14	5.17
39	5.04	5.08	5.10	5.15	5.17
38	5.33	5.36	5.43	5.50	5.50
37	5.58	5.64	5.70	5.75	5.80
36	6.02	6.09	6.17	6.19	6.27
35	6.54	6.64	6.77	6.82	6.78
34	7.25	7.38	7.48	7.67	7.68
33	7.99	8.17	8.35	8.38	8.54
32	8.90	9.05	9.29	9.45	9.59
31	9.48	9.72	9.95	10.11	10.38

Table A.7: Errors for five cases with no overlap

	Contact angles				
Rhomboid half-angle	50	60	70	80	90
45	22.46	33.49	47.25	66.52	94.35
44	21.43	32.69	46.64	66.90	93.18
43	22.59	34.27	48.10	69.36	96.20
42	22.58	33.61	48.51	68.03	96.73
41	23.46	35.29	50.01	70.96	100.26
40	19.20	31.33	45.61	66.72	95.87
39	15.40	26.56	41.69	63.55	92.10
38	16.91	28.78	46.01	69.35	99.32
37	16.56	29.32	47.41	71.06	104.88
36	18.19	32.21	51.87	76.73	114.16
35	19.49	34.89	56.99	85.72	122.87
34	21.60	38.75	62.27	97.07	140.90
33	20.93	39.89	66.24	100.47	153.35
32	19.04	38.19	67.47	108.11	167.27
31	12.27	29.36	57.88	100.28	166.92

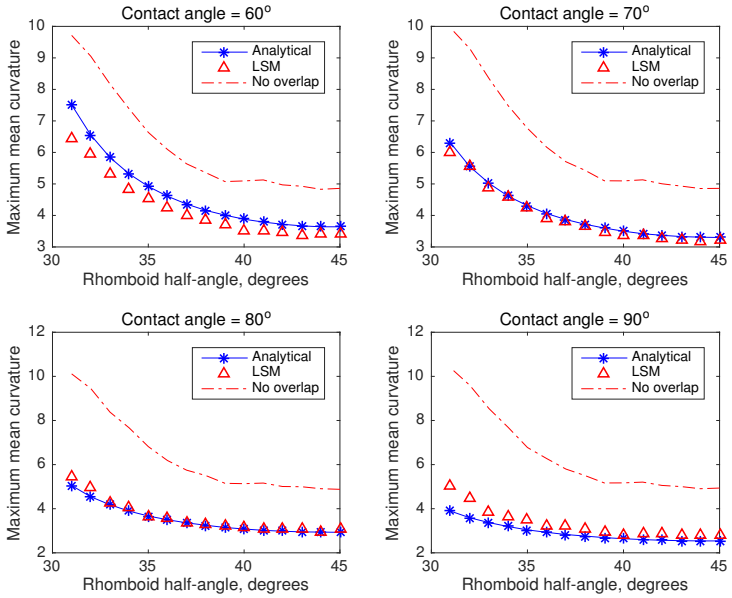

Figure A.7: Comparison of values calculated with and without overlap, for the level set method.

Appendix B. Formulae for MS-P method used by Mason and Morrow (1994)

This section briefly describes the methodology and formulae used by Mason and Morrow (1994) to derive the critical curvatures in rhomboidal pore geometries. Further details may be found in their original paper.

The calculation in [33] combined analysis of interface curvatures in a converging-diverging pore throat modeled as a toroid ring, with a pore throat formed by parallel rods and thus of a non-axisymmetric cross section. The curvatures in a converging-diverging toroidal pore throat were determined using Purcell's toroidal approximation [52]. On the other hand, for non-axisymmetric pore throats of uniform cross section, authors used the Mayer-Stowe-Princen (MS-P) theory to determine critical displacement curvatures. The validity of using MS-P theory results for a constant cross-section tube equivalent of a converging-diverging nonaxysymmetric pore throat was demonstrated experimentally for perfectly wetting liquids in [53].

Figure B.8 shows the geometry of the rhomboid pore being used (in the plane of the sphere centers), and the definitions of cell angle ϕ and inscribed circle r_i. A series of steps were devised to calculate the analytical curvatures for this geometry. In step 1, the spheres (of radius R) are replaced by rods of the same radius, at the same centers. In step 2, the MS-P curvature in the tube formed by the parallel rods is calculated for that contact angle. After that, the non-axisymmetric tube is replaced by an equivalent cylindrical tube that has the same MS-P meniscus curvature.

This tube is then used to generate a toroid, with a hole radius equal to that of the cylindrical tube, and a body radius the same as the original spheres. The MS-P curvature determined from step 2, κ_{MS-P}, gives the radius of the equivalent cylindrical tube, r_e by:

$$\frac{r_e}{R} = \frac{2cos\theta}{\kappa_{MS-P}} \tag{B.1}$$

This radius r_e sets the inner radius of the equivalent Purcell toroid, which has a body radius of R. The three-phase contact line subtends an angle α at the center of the spheres. This is referred to as the filling angle. At the position of maximum curvature in the toroid throat, the angle α^{max} is given by:

$$\alpha^{max} = \theta - sin^{-1}\left(\frac{sin\theta}{1 + (r_e/R)}\right) \tag{B.2}$$

This toroid is finally used to calculate the maximum normalized curvature κ^{max} using:

$$\kappa^{max} = \frac{2cos(\theta - \alpha^{max})}{1 + (r_e/R) - cos(\alpha^{max})} \tag{B.3}$$

These formulas were used to calculate the maximum displacement curvatures for a range of cell angles ϕ and contact angles θ, reproduced in Table A.1. It may also be noted that the case of contact angle 90° is treated separately in the paper as these formulae don't apply in that case. Figure B.9a shows the curvatures calculated versus the contact angle. Figure B.9b shows the relative meniscus curvature, normalized with the $\theta = 0°$ value, against the contact angle. This demonstrates that the maximum curvatures depend on the contact angle as $cos(\frac{2}{3}\theta)$, not as $cos\theta$. This was a significant conclusion of the paper, and has implications for upscaled implementation of contact angles.

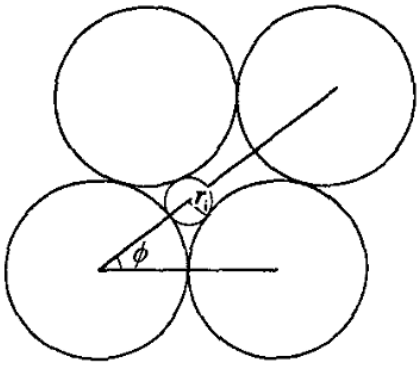

Figure B.8: Sketch of rhomboidal pore used in Morrow's experiments.

Appendix C. Convergence study for OpenFOAM

An attempt was made to improve the OpenFOAM results by refining the grid size. The grid size was halved for running these simulations. These results are presented here, with comparison with analytical values from Morrow, level set values, and those with coarses grid size. As can be seen, not much improvement is seen with these values. All simulations for contact angles 80° and 90° were not performed, and are not reported here.

In addition, we also present convergence results for two cases: rhomboid angle 45°, contact angle 10°; and rhomboid angle 30° and contact angle 90°,

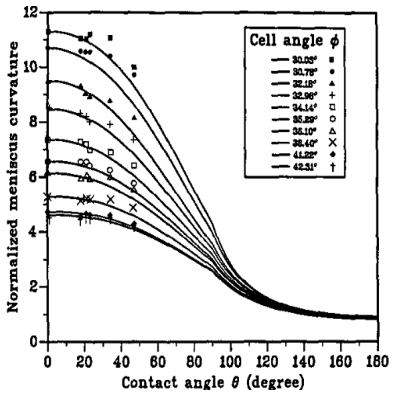

(a) Experimental results.

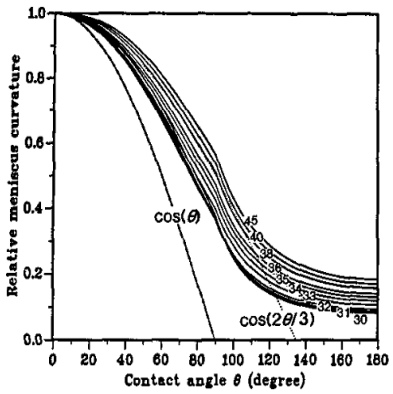

(b) Relative curvature versus contact angle.

Figure B.9: Results reprinted from Mason and Morrow [33]: maximum curvatures do not depend on the contact angle as $cos(\theta)$ (as is commonly assumed based on simplified theoretical assumptions), but as $cos(\frac{2}{3}\theta)$. Figure reprint permission is currently being processed.

with and without the damping term. Figures C.12a and C.13a show the saturation changing in the domain as we increase the capillary pressure step by step. Similarly, figures C.12b and C.13b show how the velocities have sharp jumps each time capillary pressure is increased, and then these oscillations die out towards equilibrium. The results demonstrate that the damping term stabilizes the transition to equilibrium and significantly reduces the velocity fluctuations.

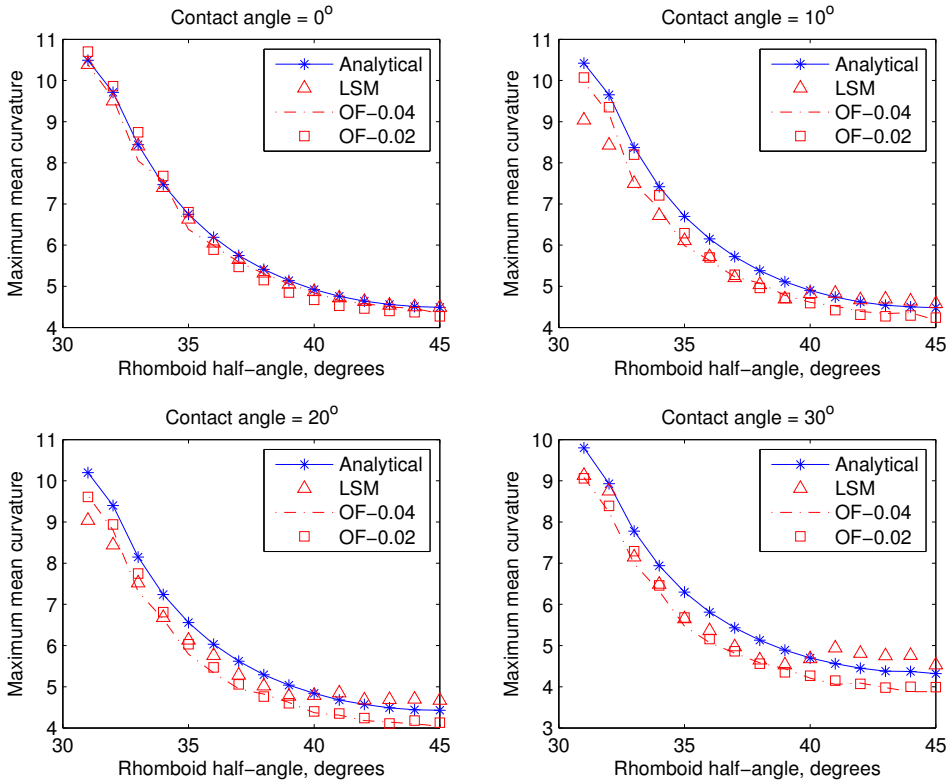

Figure C.10: Analytical vs. numerical values, incorporating values from finer grids for OpenFOAM

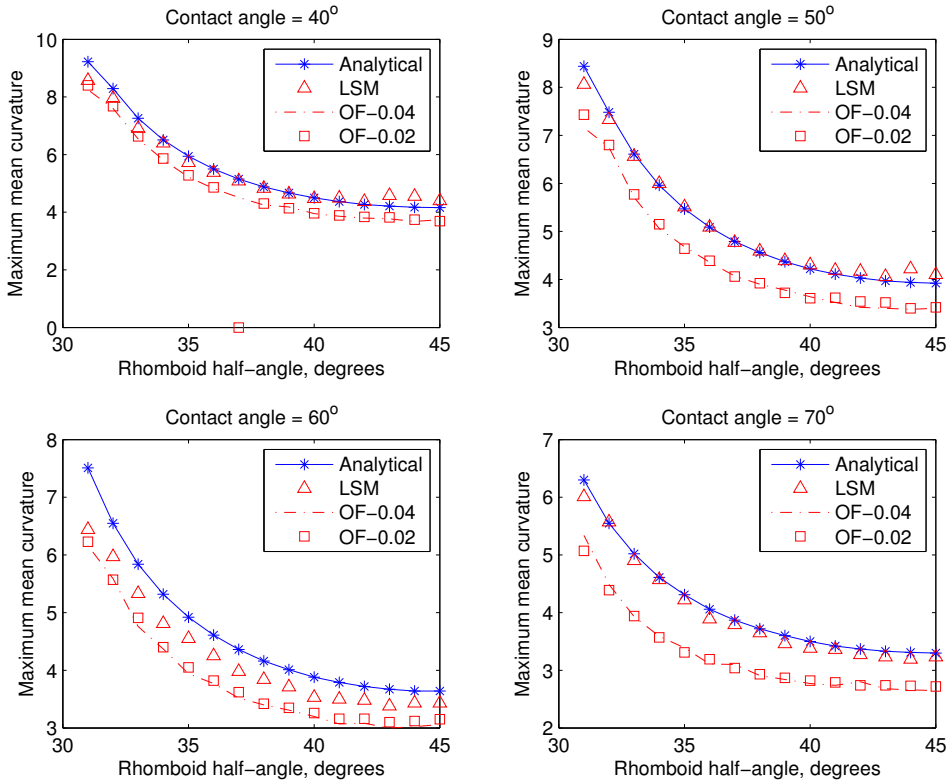

Figure C.11: Analytical vs. numerical values (continued), incorporating values from finer grids for OpenFOAM

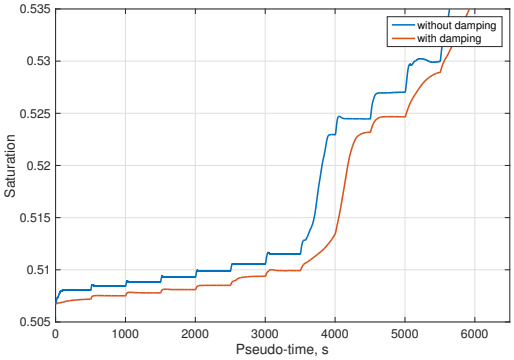

(a) Saturation convergence

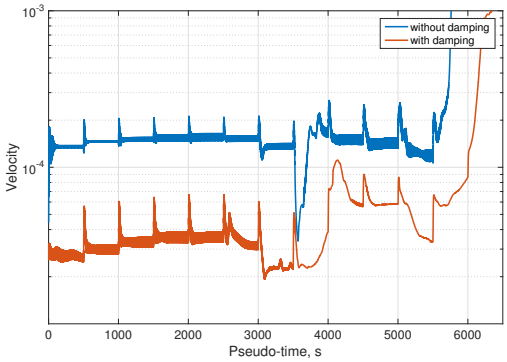

(b) Velocity convergence

Figure C.12: Comparison of saturation and velocity convergence, with and without damping, for rhomboid angle 30° and contact angle 90°.

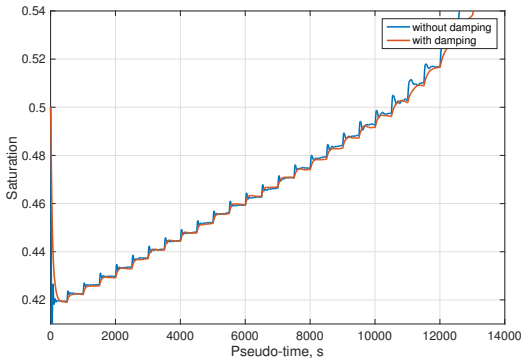

(a) Saturation convergence

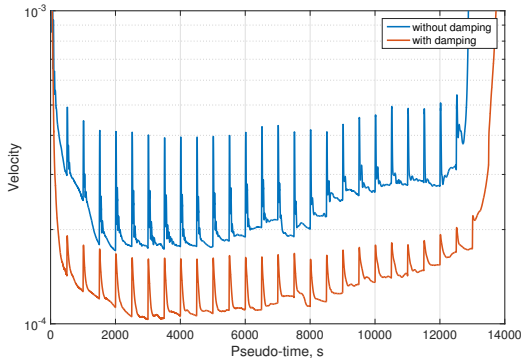

(b) Velocity convergence

Figure C.13: Comparison of saturation and velocity convergence, with and without damping, for rhomboid angle 45° and contact angle 10°.